SMM J04135+10277: a distant QSO-starburst system caught by ALMA

Citation for the original published paper (version of record):
Fogasy, J., Knudsen, K., Drouart, G. et al (2020)
SMM J04135+10277: a distant QSO-starburst system caught by ALMA
Monthly Notices of the Royal Astronomical Society, 493(3): 3744-3756
http://dx.doi.org/10.1093/mnras/staa472

Monthly Notices
of the
ROYAL ASTRONOMICAL SOCIETY

MNRAS **493,** 3744–3756 (2020)
Advance Access publication 2020 February 18

doi:10.1093/mnras/staa472

SMM J04135+10277: a distant QSO–starburst system caught by ALMA

Judit Fogasy,[1★] K. K. Knudsen,[1★] G. Drouart,[2] C. D. P. Lagos[3,4,5] and L. Fan[6,7]

[1]*Department of Space, Earth and Environment, Chalmers University of Technology, Onsala Space Observatory, SE-439 92 Onsala,*
[2]*Department of Physics and Astronomy, Curtin University, Kent Street, Bentley, Perth, WA 6102, Australia*
[3]*International Centre for Radio Astronomy Research (ICRAR), M468, University of Western Australia, 35 Stirling Hwy, Crawley, WA 6009, Australia*
[4]*ARC Centre of Excellence for All Sky Astrophysics in 3 Dimensions (ASTRO 3D)*
[5]*Cosmic Dawn Center (DAWN), Copenhagen, Denmark*
[6]*CAS Key Laboratory for Research in Galaxies and Cosmology, Department of Astronomy, University of Science and Technology of China, Hefei 230026, China*
[7]*School of Astronomy and Space Sciences, University of Science and Technology of China, Hefei, Anhui 230026, People's Republic of China*

Accepted 2020 February 12. Received 2020 February 12; in original form 2019 June 24

ABSTRACT

The gas content of galaxies is a key factor for their growth, starting from star formation and black hole accretion to galaxy mergers. Thus, characterizing its properties through observations of tracers like the CO emission line is of big importance in order to understand the bigger picture of galaxy evolution. We present Atacama Large Millimeter/submillimeter Array (ALMA) observations of dust continuum, CO(5–4) and CO(8–7) line emission in the quasar–star-forming companion system SMM J04135+10277 ($z = 2.84$). Earlier low-J CO studies of this system found a huge molecular gas reservoir associated with the companion galaxy, while the quasar appeared gas-poor. Our CO observations revealed that the host galaxy of the quasar is also gas-rich, with an estimated molecular gas mass of $\sim (0.7–2.3) \times 10^{10}\,M_{\odot}$. The CO line profiles of the companion galaxy are very broad ($\sim 1000\,km\,s^{-1}$), and show signs of rotation of a compact, massive system. In contrast to previous far-infrared observations, we resolve the continuum emission and detect both sources, with the companion galaxy dominating the dust continuum and the quasar having a ~ 25 per cent contribution to the total dust emission. By fitting the infrared spectral energy distribution of the sources with MR-MOOSE and empirical templates, the infrared luminosities of the quasar and the companion are in the range of $L_{IR,QSO} \sim (2.1–9.6) \times 10^{12}\,L_{\odot}$ and $L_{IR,Comp.} \sim (2.4–24) \times 10^{12}\,L_{\odot}$, while the estimated star formation rates are $\sim$ 210–960 and $\sim$ 240–2400 $M_{\odot}\,yr^{-1}$, respectively. Our results demonstrate that non-detection of low-J CO transition lines in similar sources does not necessarily imply the absence of massive molecular gas reservoir but that the excitation conditions favour the excitation of high-J transitions.

Key words: galaxies: active – galaxies: evolution – galaxies: high-redshift – galaxies: starburst – submillimetre: galaxies – galaxies: individual: SMM J04135+10277.

1 INTRODUCTION

An intense phase of star formation and supermassive black hole (SMBH) growth at high-redshift is necessary to explain the observed correlation found in local elliptical galaxies between the mass of the SMBH and some properties of the host galaxy, such as the velocity dispersion or bulge mass (e.g. Magorrian et al. 1998; Gebhardt et al. 2000; Merritt & Ferrarese 2001; Tremaine et al. 2002; Marconi & Hunt 2003; Häring & Rix 2004; McConnell & Ma 2013). The found correlations suggest that the evolution of the SMBHs and their host galaxies are tied together. Theoretical studies of galaxy evolution provide a possible framework for this co-evolution in form of interactions and major merger events between massive and gas-rich galaxies (e.g. Sanders et al. 1988; Di Matteo, Springel & Hernquist 2005; Di Matteo et al. 2008; Hopkins et al. 2008, 2006; Narayanan et al. 2010). As the star formation and black hole activity peaks at around $z \sim 2–3$ (e.g. Madau, Pozzetti & Dickinson 1998; Hopkins 2004; Richards et al. 2006; Zheng et al. 2009; Aird et al. 2010, 2015), by probing the far-infrared (FIR) properties and molecular gas content of high-z active galactic nuclei (AGNs) and their close environment, we can probe this scenario. Moreover, there is an extensive literature with ambiguous conclusions on whether there is a strong correlation between the star formation rate (SFR) and AGN luminosity of high-redshift AGNs (e.g. Schweitzer et al. 2006; Lutz et al. 2010; Bonfield et al. 2011; Mullaney et al. 2012; Santini et al. 2012; Stanley et al. 2015; Bernhard et al. 2016; Dong &

★ E-mail: judit.fogasy@chalmers.se (JF); kirsten.knudsen@chalmers.se (KKK)

Wu 2016; Netzer et al. 2016; Pitchford et al. 2016; Duras et al. 2017; Ramasawmy et al. 2019; Schulze et al. 2019). Based on these studies the growth of AGNs can follow two different paths: low or moderate luminosity AGNs can evolve through secular processes, thus the SMBH growth is not directly linked to the star formation of the host galaxy; while the most luminous AGNs grow through major mergers which enhance the star formation of the hosts.

Indeed, in the last decade several quasar studies at submm wavelength found signs of intense star formation in their hosts by tracing dust continuum emission and [C II] cooling line emission (e.g. Carilli et al. 2001; Omont et al. 2001; Maiolino et al. 2005; Wang et al. 2013; Venemans et al. 2016). However, most of these studies are limited in resolution and/or sensitivity, thus they could miss the detection of close companion galaxies, which also have a contribution to the submm emission.

Thanks to the high angular resolution and sensitivity of the Atacama Large Millimeter/submillimeter Array (ALMA), many recent studies of high-z quasars found companion galaxies in their vicinity, in some cases more than one (e.g. Wagg et al. 2012; Carilli et al. 2013; Silva et al. 2015; Banerji et al. 2017, 2018; Carniani et al. 2017; Decarli et al. 2017; Trakhtenbrot et al. 2017; Fan et al. 2018). These results are in agreement with our earlier study, where we used GALFORM (Gonzalez-Perez et al. 2014; Lagos et al. 2014), a galaxy formation and evolution model with the aim of investigating the expected frequency of finding quasar–companion galaxy systems (Fogasy et al. 2017).

In this paper, we focus on the quasar–star-forming companion galaxy system SMM J04135+10277 ($z = 2.84$). The AGN component of the system is a type-1 quasar, originally discovered at submm wavelength (Knudsen, van der Werf & Jaffe 2003) using the Submillimetre Common-User Bolometer Array (SCUBA). Subsequent single-dish observations of the quasar tracing low-J CO transitions revealed a massive molecular gas reservoir associated with the AGN ($M_{\rm H_2} \sim 10^{11} {\rm M}_\odot$; Hainline et al. 2004; Riechers et al. 2011b). However, follow-up interferometric observations showed that the gas reservoir was offset from the position of the quasar by ∼5 arcsec (41.5 kpc) and associated with a close companion galaxy (Riechers 2013). Both the quasar and its companion are slightly gravitationally lensed by the foreground galaxy cluster Abell 478, by a gravitational magnification factor of $\mu_{\rm QSO} = 1.3$ and $\mu_{\rm Comp.} = 1.6 \pm 0.5$, respectively (Knudsen et al. 2003; Riechers 2013). Given the molecular gas distribution and the separation between the sources, the system has been proposed to be in an early stage of a wet-dry merger event, the companion being gas-rich and the quasar being gas-poor, making this case unique (Riechers 2013). Based on the spectral energy distribution (SED) of the companion galaxy we can infer that it is a heavily dust-obscured star-forming galaxy ($A_{\rm V} \sim 2.8$ mag), with an SFR of $\sim 700\,{\rm M}_\odot\,{\rm yr}^{-1}$ and dust mass of $\sim 5 \times 10^9\,{\rm M}_\odot$ (Fogasy et al. 2017). Considering the high SFR, molecular gas and dust mass of the companion galaxy, it is possible that the companion has a significant contribution to the SCUBA detected submm emission and the majority of star formation happens in the companion rather than in the host galaxy of the quasar.

In order to further investigate this system we obtained dust continuum, CO(5–4) and CO(8–7) observations with ALMA. Our goal is to constrain the excitation properties of SMM J04135+10277 through modelling of the spectral line energy distribution (SLED) of both sources and to deepen our understanding of the processes shaping the evolution of this system. This is important because prior to ALMA, the majority of studies finding AGN–companion systems were focusing on the large-scale environment of AGNs and did not study the systems in details.

In Section 2, we present the ALMA observations, in Section 3 we describe the results of the observations and the data analysis, including the SLED modelling of the sources. In Section 4, we discuss our findings and compare them with other studies found in the literature. Finally, we summarise our results in Section 5. Throughout this paper we adopt WMAP7 cosmology with $H_0 = 70.4\ {\rm km\ s^{-1} Mpc^{-1}}$, $\Omega_{\rm m} = 0.272$, and $\Omega_\Lambda = 0.728$ (Komatsu et al. 2011).

Table 1. Details of the ALMA observations of SMM J04135+10277.

	Band 4	Band 6
Date	2016-06-02	2016-03-31
Configuration	C40-4	C36-2/3
$N_{\rm antennas}$	37	44
$T_{\rm exp}$ (min)	10.6	10.1
Beam size (arcsec)	1.01 × 0.92	1.0 × 0.78
$\rm RMS_{cont.}$ (μJy beam^{-1})	27.8	46.7
$\rm RMS_{line}$ (mJy beam^{-1})[a]	0.32	0.38

[a]The spectra are binned to 77 km s^{-1} in each band.

2 OBSERVATIONS

SMM J04135+10277 was observed with the 12 m ALMA array during cycle 3 (project code 2015.1.00661.S; PI: Fogasy). One of the spectral windows with a bandwidth of 1.875 GHz was tuned to the central frequency of 149.843 GHz to cover the redshifted CO(5–4) line in band 4, and to 239.648 GHz to cover the redshifted CO(8–7) line in band 6. The other three spectral windows of each band, with a bandwidth of 2 GHz each, were used to observe the continuum. Other details of the observations are given in Table 1.

The calibration of the data was done using the ALMA Science Pipeline. The calibration process includes standard calibration and reduction steps, such as flagging, bandpass calibration, flux, and gain calibration. The quasar J0423−0120 was used as a bandpass calibrator source. Due to the strong variability of the flux calibrator source at the time of the observations (∼ 10 per cent in both bands), the flux calibration was redone with updated flux values. After this correction we assume a conservative 10 per cent absolute flux calibration error, which is not included in the flux densities reported in this paper.

To image the data we used the Common Astronomy Software Applications (CASA; McMullin et al. 2007) with the ARC Node provided scripts. We applied the CLEAN algorithm to create the continuum images and line data cubes using natural weighting. In case of the spectral line data, the continuum was fitted using the line free channels of every spectral window and was subtracted in the *uv*-plane using the UVCONTSUB task in CASA. For each band the continuum subtracted line data was imaged with 77 km s^{-1} channel width.

3 RESULTS AND ANALYSIS

3.1 Dust continuum emission, FIR luminosities, and star formation rates

The ALMA observations enabled us to resolve the FIR emission of SMM J04135+10277 and detect both sources for the first time (Fig. 1), in contrast to previous single-dish submm observations,

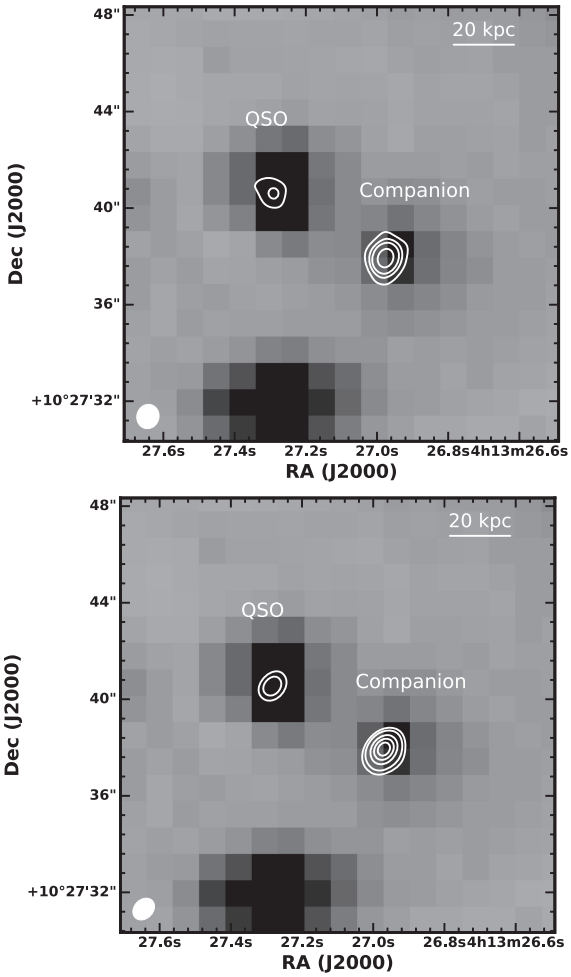

Figure 1. ALMA 150 GHz (*upper panel*) and 240 GHz (*lower panel*) dust continuum contours overlayed on the *Spitzer* IRAC 4.5 μm image of SMM J04135+10277. The beam size is indicated in the bottom left corner. The contour levels are 5σ, 10σ, 15σ, 25σ for the 150 GHz continuum and 25σ, 50σ, 75σ, 100σ for the 240 GHz continuum.

Table 2. Positions, continuum fluxes, and physical source sizes of the system of SMM J04135+10277.

	QSO	Companion
RA	04:13:27.28	04:13:26.98
Dec.	+10:27:40.41	+10:27:37.89
$S_{150\,\mathrm{GHz}}$ (mJy)	0.399 ± 0.015	1.233 ± 0.037
$S_{240\,\mathrm{GHz}}$ (mJy)	2.174 ± 0.023	7.64 ± 0.30
Size at 150 GHz (arcsec)	0.67×0.32	0.71×0.44
Size at 240 GHz (arcsec)	0.53×0.37	0.65×0.45

where the quasar and its companion remained unresolved within a single beam (e.g. SCUBA beam is 15 arcsec at 850 μm, the separation between the quasar and the companion is ∼5 arcsec). Thanks to the high sensitivity of ALMA we achieved a robust detection, yielding a high signal-to-noise ratio of 14 and 46 in the case of the quasar and 44 and 163 in the case of the companion galaxy, in band 4 and band 6, respectively. The dust emission of the quasar is much weaker compared to the companion galaxy, only about 22–25 per cent of the total emission in both bands (Table 2). In band 4, the cD galaxy of A478 is detected north-west from the phase centre (RA $= 04^{\mathrm{h}}13^{\mathrm{m}}25\overset{\mathrm{s}}{.}27$, Dec. $= +10^{\circ}27'54\overset{''}{.}69$), at ∼33 arcsec (∼ 264 kpc) distance from the quasar but it is not detected in the band 6 data.

The UV-to-IR SED of the companion galaxy was constructed in Fogasy et al. (2017), here we focus on the FIR SED of the quasar and the companion. To complement our ALMA observations we used previous SCUBA and ArTeMiS data to obtain the SED (Knudsen et al. 2003; Fogasy et al. 2017). As the resolution of the single-dish data is not sufficient to separate emission associated with the quasar and the companion galaxy, we use the multiwavelength SED fitting code MR-MOOSE (Drouart & Falkendal 2018). The code is designed to treat upper limits consistently as well as large variations of resolution and to fit blended sources using a Bayesian framework, by allowing the user to use the spatial information. MR-MOOSE simultaneously fits the SEDs of the quasar and the companion, and the total emission when it is impossible to resolve sources individually, e.g. in the SCUBA bands. The best-fitting models and the possible range of solutions are shown in Fig. 2. In the case of the quasar the dust emissivity and dust temperature of the best-fitting model are $\beta_{\mathrm{dust,\,QSO}} = 2.5 \pm 0.3$ and $T_{\mathrm{dust,QSO}} = 24 \pm 6$ K. In the case of the companion the best-fitting model predicts $\beta_{\mathrm{dust,\,Comp.}} = 3.3 \pm 0.4$ and $T_{\mathrm{dust,Comp.}} = 16 \pm 3$ K. Considering the small number of available data points, it is difficult to properly constrain the absolute values of β and T_{dust}, but the MR-MOOSE result still highlights that the quasar has a consistently higher temperature compared to the companion.

The FIR luminosities of the quasar and its companion based on the best-fitting MR-MOOSE SED models are $L_{\mathrm{FIR,QSO}} = (2.1^{+1.7}_{-1.2}) \times 10^{12}\,\mathrm{L}_{\odot}$ and $L_{\mathrm{FIR,Comp.}} = (2.4 \pm 1) \times 10^{12}\,\mathrm{L}_{\odot}$, corrected for gravitational lensing magnification. From the obtained infrared luminosities, the SFR of the sources can be estimated according to the relation $\mathrm{SFR} \sim \delta_{\mathrm{MF}} \times 10^{-10}\,L_{\mathrm{IR}}$ (Carilli & Walter 2013), assuming that the dust is heated by star formation. As MR-MOOSE only fits the FIR part of the SED, the total IR luminosity of the sources could be higher. Thus, we treat the SFR calculated from the L_{FIR} as a lower limit. By adopting a Chabrier initial mass function ($\delta_{\mathrm{MF}} \sim 1$), we get an SFR of ∼ 210 and ∼ 240 $\mathrm{M}_{\odot}\,\mathrm{yr}^{-1}$ for the quasar and the companion, respectively.

In addition, we used the empirical SED model grid of Chary & Elbaz (2001) as an alternative approach to fit the IR SED of quasar and the companion. The grid includes 105 templates with a wide range of infrared luminosities. As the SED templates have no free parameters, we chose the templates that fit our ALMA detections the best. For the SCUBA bands we assumed a 25 per cent contribution from the quasar, based on the ALMA detections. The best-fitting templates are shown in Fig. 2 together with the MR-MOOSE models. Based on the best-fitting Chary & Elbaz (2001) templates the IR luminosities of the quasar and the companion are $L_{\mathrm{IR,QSO}} \sim 9.6 \times 10^{12}\,\mathrm{L}_{\odot}$ and $L_{\mathrm{IR,Comp.}} \sim 2.4 \times 10^{13}\,\mathrm{L}_{\odot}$ (the luminosities are corrected for the gravitational lensing magnification). The SFR of the quasar and its companion according the same relation as above is ∼ 960 and ∼ 2400 $\mathrm{M}_{\odot}\,\mathrm{yr}^{-1}$, respectively.

By comparing the results of the two approaches, the Chary & Elbaz (2001) templates cannot fit well the data unless the quasar's contribution at the 450 μm SCUBA wavelength is higher (∼ 35 per cent). Furthermore, the Chary & Elbaz (2001) templates are constructed for low-redshift star-forming galaxies and might not be suitable for high-z AGNs. As MR-MOOSE only fits a modified-blackbody SED to the FIR part of the SED and the Chary & Elbaz (2001) templates cover the whole luminosity, the results of these

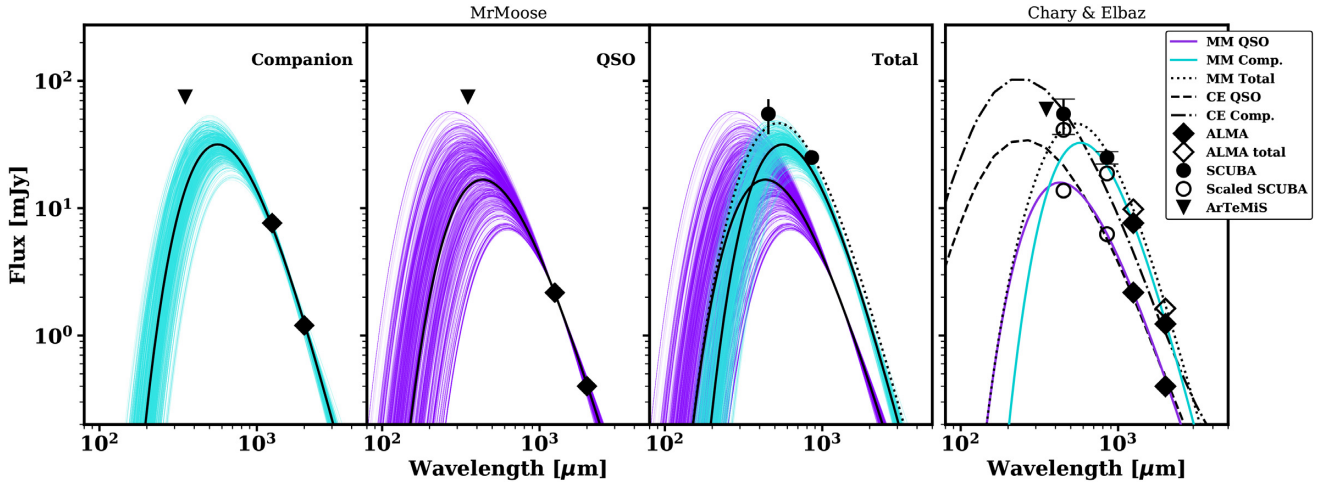

Figure 2. The FIR SED of the quasar and its companion. The first three panels show the MR-MOOSE modified blackbody SED of the companion, the quasar and the total emission, respectively. The purple and turquoise lines show the possible range of solutions. The third panel shows the MR-MOOSE best-fitting models of the quasar and the companion (solid lines), and the total emission (dotted line). The fourth panel shows the best-fitting MR-MOOSE SEDs as turquoise, purple, and dotted lines, and the best-fitting Chary & Elbaz (2001) SED of the quasar and the companion (dashed and dash–dotted lines). On all panels the symbols represent the same observations. The black diamonds represent the ALMA observations; the black unfilled diamonds show the total ALMA emission of the quasar and the companion. The black circles show the total SCUBA 450 and 850 μm emission; the black unfilled circles represent the SCUBA observations, scaled by the assumed relative contribution of the quasar (25 per cent) and companion (75 per cent) to the total emission. The upper limit shows the 3σ ArTeMiS measurement of the system.

two approaches can be treated as lower and upper limits for the total IR luminosity and the SFR of the sources.

3.2 CO(5–4) and CO(8–7) line emission

We detect CO(5–4) and CO(8–7) line emission from both the quasar and the companion galaxy (Figs 3 and 4). As it was expected from earlier CO(1–0) and CO(3–2) observations, both the CO(5–4) and CO(8–7) emission is dominated by the companion galaxy. However, while the quasar remained undetected at low-J CO transitions, it appears bright in our high-J transition observations. This indicates that the host galaxy of the quasar has a significant amount of warm, highly excited molecular gas.

The line emitting regions of both sources are compact and in the case of the companion, we do not see the elongated shape previously found by Riechers (2013). For further inspection, the spectra of the quasar and companion were extracted from the line data cube. We fitted the spectra using Gaussian line profiles in order to determine the line widths and velocity integrated fluxes of the sources.

The CO line profiles of the quasar are narrow and shifted by $\sim 700\,\mathrm{km\,s^{-1}}$ with respect to the redshift of the quasar derived from rest-frame ultraviolet emission lines ($z_{\mathrm{UV}} = 2.837 \pm 0.003$; Knudsen et al. 2003). This is in agreement with previous studies of high-redshift quasars, which found that the broad UV emission lines of quasars tend to be blueshifted by several hundreds of $\mathrm{km\,s^{-1}}$ compared to emission lines probing the interstellar medium of the host galaxies, such as the [C II] and CO lines (e.g. Riechers 2011; Willott, Bergeron & Omont 2015; Venemans et al. 2016; Trakhtenbrot et al. 2017; Decarli et al. 2018).

In contrast, the CO(5–4) and CO(8–7) line profiles of the companion are very broad, 1127 ± 49 and $1038 \pm 110\,\mathrm{km\,s^{-1}}$ respectively, when fitting a single Gaussian profile. There is a discrepancy between the line widths of the different CO transitions: the CO(1–0) and CO(3–2) lines are narrower (679 ± 120 and $765 \pm 222\,\mathrm{km\,s^{-1}}$; Riechers 2013; Sharon et al. 2016) compared to the higher J transition lines reported here. The fitted CO redshifts of the companion shown in Table 3 are consistent within the uncertainties of the CO(1–0) redshift reported in Sharon et al. (2016) and slightly lower compared to the CO(3–2) redshift presented in Riechers (2013), which we attribute to the much higher signal-to-noise ratio of our measurements.

3.3 CO kinematic properties of the companion

For the companion galaxy, the ALMA observations reveal that the emission of the CO(5–4) and CO(8–7) line is spatially extended over a few beams, though less than suggested in Riechers (2013). We analysed the intensity weighted velocity field map (moment-1 map), the velocity dispersion map (moment-2) and the position–velocity (PV) diagram of the source to characterise the kinematic properties and understand the discrepancy between the linewidth of the low-J and high-J data (Fig. 5). For the PV diagram we chose the angle towards the highest velocity gradient ($-30°$) and used the same angle for both transitions. The position and angle from which the PV diagram was derived is indicated as a blue line in Fig. 5. The velocity map and the PV diagram of the CO(8–7) emission line are less well defined compared to that of the CO(5–4) line, which might be the result of the lower signal-to-noise ratio achieved in band 6. Both the velocity field maps and the PV diagrams of the high-J transition lines show that the emission is consistent with rotation of a massive and compact system with maximal velocity values of $|V_{\mathrm{max}} \sin i| \gtrsim 300\,\mathrm{km\,s^{-1}}$ and show no clear signs of outflows, despite the very broad linewidth. The velocity dispersion maps of the companion show very high dispersion across the source. A common characteristic of rotating systems is an increase of the velocity dispersion towards the centre. The resolution of the natural weighted image is insufficient to show this, and beam smearing could cancel

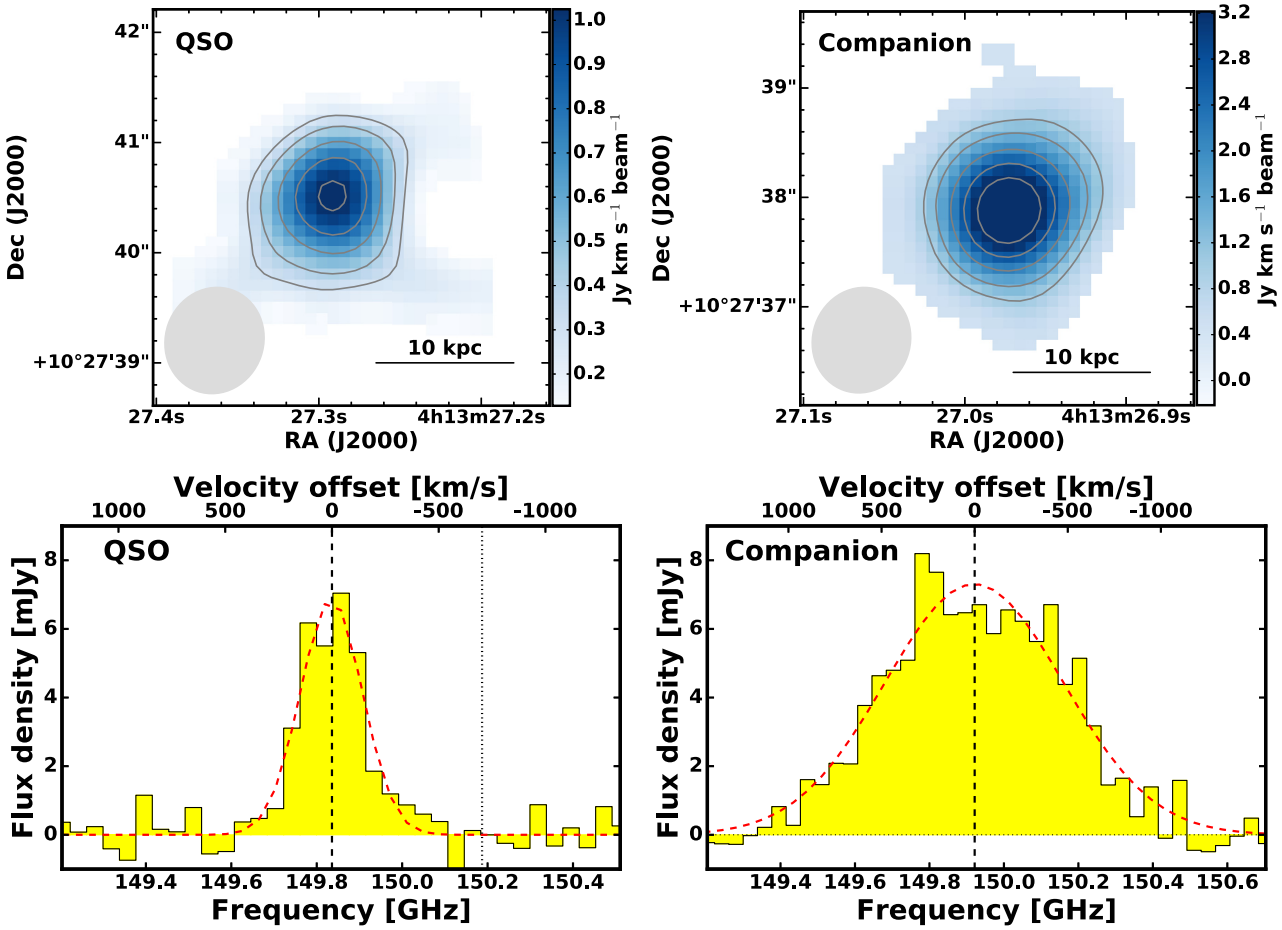

Figure 3. CO(5–4) emission of the system of SMM J04135+10277. *Top:* Integrated intensity contour maps of the quasar and its companion. The contour levels are at [5, 7, 10, 13, 16] $\times\ \sigma$, where $\sigma = 0.064\,\mathrm{Jy\,beam^{-1}\,km\,s^{-1}}$ for the QSO and $\sigma = 0.214\,\mathrm{Jy\,beam^{-1}\,km\,s^{-1}}$ for the companion. ALMA beams are shown as grey ellipses at the bottom left corner. *Bottom:* The CO(5–4) spectra of SMM J04135+10277 extracted at the position of the quasar and the companion galaxy, respectively. The spectra are binned to 77 km s^{-1} per channel and the continuum is subtracted. The red curves show the single component Gaussian fits to the line profiles. The vertical dashed lines indicate the redshifts of the quasar and the companion obtained from the line fitting of the CO(5–4) emission lines. The vertical dotted line indicate the optical redshifts of the quasar ($z = 2.837$; Knudsen et al. 2003). The top-axis shows the relative velocity offset with respect to the fitted redshifts.

out this feature. Thus, a proper analysis of the kinematics is not possible given that several resolution elements would be needed on either side of a potential rotation curve (e.g. Epinat et al. 2010; Di Teodoro & Fraternali 2015). However, in Appendix A we present a simple kinematic model with rotation using GalPak^{3D} (Bouché et al. 2015).

In contrast to the companion galaxy, the quasar host galaxy does not display a complex line profile and signs of a velocity gradient, hence we do not carry out a similar analysis for this source. In Appendix B, we present the moment-1 and moment-2 maps of the quasar.

3.4 CO line luminosities and gas masses

The CO(5–4) and CO(8–7) line luminosities are derived using the following equation from Solomon et al. (1997): $L'_{\mathrm{CO}} = 3.25 \times 10^7 \times S_{\mathrm{CO}}dV \times \nu_{\mathrm{obs}}^{-2} \times D_{\mathrm{L}}^2 \times (1+z)^{-3}$, where $S_{\mathrm{CO}}dV$ is the velocity integrated flux, ν_{obs} is the observed frequency of the line in GHz and D_{L} is the luminosity distance in Mpc. The derived luminosities of the sources are corrected for the gravitational lensing and are summarized in Table 3.

To estimate the molecular gas mass of the system, we use the CO(5–4) line observations together with the CO(1–0) line observations of Sharon et al. (2016). We take this approach as the molecular gas mass is best estimated from the ground transition of CO and for the companion interferometric CO(1–0) detection is available, while the quasar is only detected in our higher J ALMA observations. In the further analysis, we adopt a conversion factor of $\alpha_{\mathrm{CO}} = 0.8\,\mathrm{M_\odot\,(K\,km\,s^{-1}\,pc^2)^{-1}}$ (Downes & Solomon 1998), which is typically used for starburst galaxies.

In the case of the companion, Sharon et al. (2016) reported a line luminosity of $L'_{\mathrm{CO(1-0)}} = (8.6 \pm 1.7) \times 10^{10}\,\mathrm{K\,km\,s^{-1}\,pc^2}$, which converts to a molecular gas mass of $(6.8 \pm 1.4) \times 10^{10}\,\mathrm{M_\odot}$. This is about a factor of 2 lower than the molecular gas mass determined by Riechers (2013), and can be a result of the different resolution of the observations. Regardless of this difference, it is clear that the companion has a massive gas reservoir.

The quasar was not detected by Sharon et al. (2016) but a 3σ upper limit is obtained, yielding a CO(1–0) line luminosity upper limit of $1.9 \times 10^{10}\,\mathrm{K\,km\,s^{-1}\,pc^2}$, which converts to a molecular gas mass of $7.4 \times 10^9\,\mathrm{M_\odot}$. We also calculated the molecular gas mass from the CO(5–4) emission of the quasar, as this is the lowest J

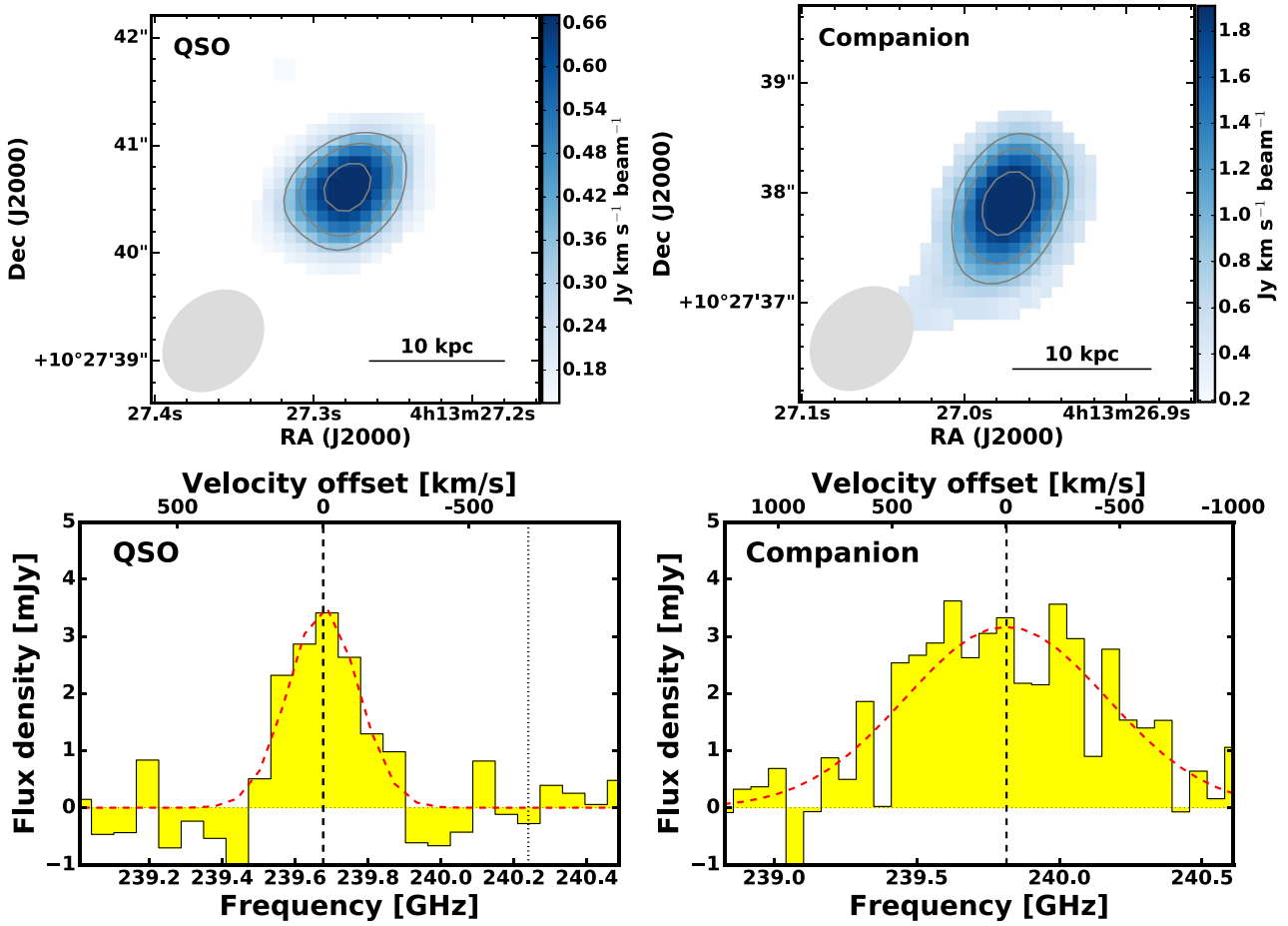

Figure 4. CO(8–7) emission of the system of SMM J04135+10277. *Top:* Integrated intensity contour maps of the quasar and its companion. The contour levels are at [5, 7, 10] × σ, where $\sigma = 0.067$ Jy beam^{-1} km s^{-1} for the QSO and $\sigma = 0.191$ Jy beam^{-1} km s^{-1} for the companion. ALMA beams are shown as grey ellipses at the bottom left corner. *Bottom:* The CO(8–7) spectra of SMM J04135+10277 extracted at the position of the quasar and the companion galaxy, respectively. The spectra are binned to 77 km s^{-1} per channel and the continuum is subtracted. The red curves show the single component Gaussian fits to the line profiles. The vertical dashed lines indicate the redshifts of the quasar and the companion obtained from the line fitting of the CO(8–7) emission lines. The vertical dotted line indicate the optical redshifts of the quasar ($z = 2.837$; Knudsen et al. 2003). The top-axis shows the relative velocity offset with respect to the fitted redshifts.

Table 3. Velocity integrated fluxes, line widths, and line luminosities of the system of SMM J04135+10277.

	QSO	Companion
$SdV_{CO(5-4)}$ (Jy km s^{-1})	2.50 ± 0.22	8.77 ± 0.50
$SdV_{CO(8-7)}$ (Jy km s^{-1})	1.04 ± 0.18	3.50 ± 0.49
$FWHM_{CO(5-4)}$ (km s^{-1})	340 ± 23	1127 ± 49
$FWHM_{CO(8-7)}$ (km s^{-1})	278 ± 37	1038 ± 110
$z_{CO(5-4)}$	2.8460 ± 0.0001	2.8438 ± 0.0003
$z_{CO(8-7)}$	2.8460 ± 0.0002	2.8438 ± 0.0006
$L'_{CO(5-4)}{}^{a}$ (10^{10} K km s^{-1} pc^2)	2.9 ± 0.3	8.3 ± 0.5
$L'_{CO(8-7)}{}^{a}$ (10^{10} K km s^{-1} pc^2)	0.5 ± 0.8	1.3 ± 0.2

[a]The luminosities are corrected for gravitational lensing magnification: $\mu_{QSO} = 1.3$ (Knudsen et al. 2003); $\mu_{Comp.} = 1.6$ (Riechers 2013).

detection available for this source. We assume that the CO(5–4) transition is thermally excited, based on CO(4–3) observations of high-z type I QSOs, which found a unity $L'_{CO(4-3)}/L'_{CO(1-0)}$ ratio (e.g. Riechers et al. 2006; Weiß et al. 2007). With this assumption the molecular gas mass of the quasar is $(2.3 \pm 0.2) \times 10^{10}$ M$_\odot$. These results suggest that there is a significant amount of warm gas in the quasar and it cannot be considered gas-poor.

3.5 RADEX modelling of the CO spectra

To put constraints on the excitation properties of SMM J04135+10277, we modelled the SLED of both sources using our ALMA detections combined with CO(1–0) and CO(3–2) line observations from the literature (Riechers 2013; Sharon et al. 2016). We used the non-LTE molecular radiative transfer code RADEX (van der Tak et al. 2007) to calculate the line intensities of CO from transitions $J_{up} = 1$ to $J_{up} = 8$, within a wide range of physical parameters: kinetic temperature (T_{kin}), number density of molecular hydrogen (n_{H_2}), and column density of CO (N_{CO}). During each run we set the background radiation temperature to the value of the cosmic microwave background at $z = 2.84$, adopted spherical geometry and assumed that the only collisional partner of CO is molecular hydrogen. As the linewidths of the low- and high-J CO lines are different, we use an average value during the RADEX modelling. The RADEX code only considers photodissociation regions and does not include mechanical and X-ray heating. We compared our observations with the models using

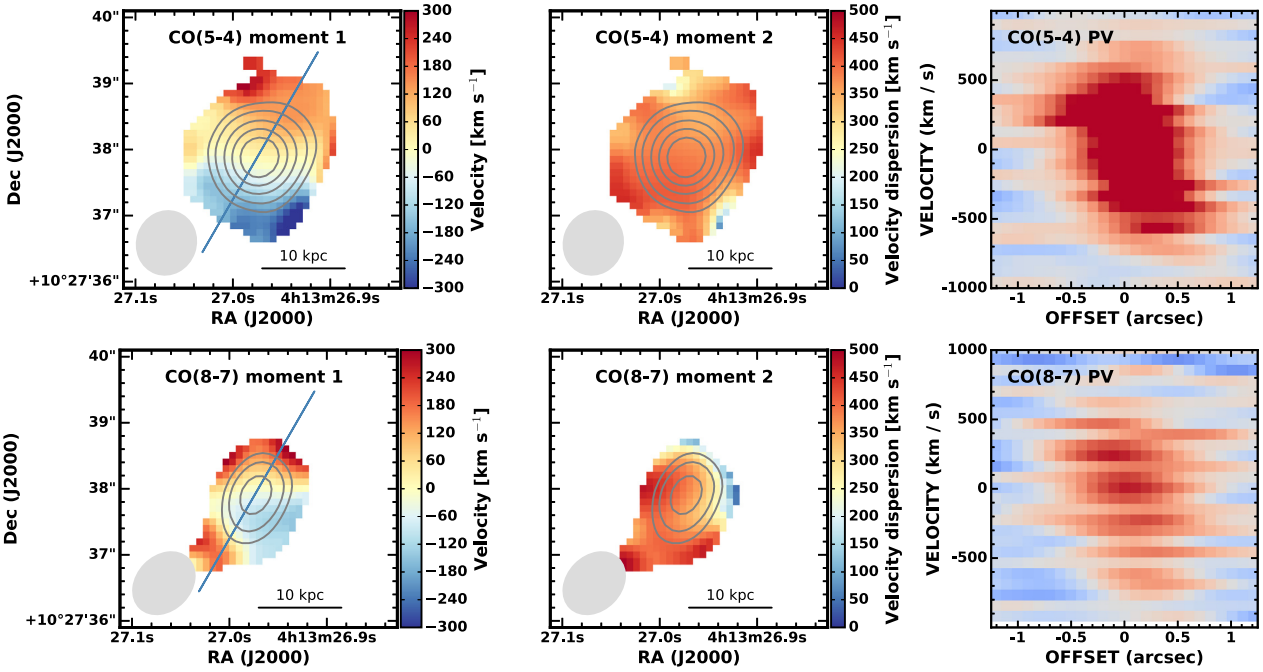

Figure 5. Kinematics of the companion galaxy. *Left:* The velocity map of the companion galaxy. The blue line indicates the position and angle from which the PV diagram was derived. *Middle:* The velocity dispersion map of the companion galaxy. *Right:* The PV diagram of the companion galaxy. Top and bottom rows show the results for the CO(5–4) and the CO(8–7) line, respectively. Contours trace the integrated line intensity with contour levels same as in Fig. 3 for the CO(5–4) emission and Fig. 4 for the CO(8–7) emission.

χ^2-analysis. In the first run we varied all three physical parameters in case of each source but as most of the models converged to the same CO column density, we fixed $N_{\rm CO}$ and continued with fitting only $T_{\rm kin}$ and $n_{\rm H_2}$.

During the RADEX modelling of the quasar we set the line width of 300 km s^{-1}, fixed $N_{\rm CO}$ to 10^{16} cm^{-2} and run RADEX on a grid of $T_{\rm kin}$ = [10–400] K and $\log(n_{\rm H_2})$ = [2–7] cm^{-3}. It is important to note, that as we only have two detections for the quasar and two upper limits, we do not expect to arrive to a straightforward conclusion about the excitation properties of this source. However, by using the available data we can narrow down the possible temperature and density ranges.

Fig. 6 shows how the χ^2 value of the models vary as a function of temperature and density. The upper J transitions of the quasar can be fitted by models with a continuous range of kinetic temperatures of 60–400 K and molecular hydrogen density between 10^4 and $10^{6.2}$ cm^{-3}. Models with the lowest χ^2 values are outside of the typical temperature range for quasars ($T_{\rm kin}$ = 40–60 K; Riechers et al. 2006, 2009; Carilli & Walter 2013) and the corresponding densities are much higher compared to the typical quasar value ($10^{3.6}$–$10^{4.3}$ cm^{-3}). This might be due to the lack of data points to produce a reasonable fit but it could also suggest the presence of an extremely compact region of highly excited gas close to the central AGN. In contrast, there are models with low χ^2 value and densities within the typical range for quasars but their temperature is not well constrained. In order to illustrate how the RADEX models fit the observations, in Fig. 7 we plot three model SLEDs with low χ^2 value but with different temperatures and densities. In addition, we calculated the molecular gas mass of the quasar using the CO(1–0) line intensity of the best-fitting models, which gives a mass range of (1.2–1.8) $\times$ 10^9 M$_\odot$. The RADEX estimated gas mass is lower compared to the gas mass derived from the CO(5–4) transition and the CO(1–0) upper limit.

For the modelling of the companion galaxy we used a line width of 850 km s^{-1}, fixed $N_{\rm CO}$ to 10^{17} cm^{-2} and run RADEX on a grid of $T_{\rm kin}$ = [10–400] K and $\log(n_{\rm H_2})$ = [2–7] cm^{-3}. From the χ^2-analysis we found that models with low χ^2 value give a consistent estimate for the molecular hydrogen density, between 10^3 and 10^4 cm^{-3}, but can have temperatures ranging from 110 to 400 K (Fig. 6). While the temperatures of the best-fitting models are not well constrained, they could narrow down the possible molecular hydrogen density range of the companion, and the yielded range is within the typical values found for submillimetre galaxies (SMGs) ($10^{2.7}$–$10^{3.5}$ cm^{-3}; Carilli & Walter 2013). Using the CO(1–0) line intensity of the best-fitting models, the molecular gas mass of the companion is (2.9–4.5) $\times$ 10^{10} M$_\odot$, which is fairly close to the gas mass derived from the CO(1–0) transition. In Fig. 7, we show three models SLEDs which have low χ^2 value, but have very different kinetic temperatures. Based on Fig. 7 it is clear that even the best-fitting RADEX models cannot fit well the data and the temperature cannot be simply constrained.

4 DISCUSSION

4.1 FIR emission of SMM J04135+10277

Thanks to the high-resolution of ALMA we were able to resolve the system of SMM J04135 and detect FIR emission from both the quasar and its companion. However, fitting the FIR SED of the sources is still challenging, as the ALMA observations only trace emission at the Rayleigh–Jeans side of the FIR SED and adequate observations around the peak of the FIR SED are lacking. It has been shown that the wavelength of the rest-frame SED peak can be used as a proxy for dust temperature and it decreases with increasing total infrared luminosity but it is dependent on the emissivity and opacity of the used model (Lee et al. 2013). Furthermore, the dust

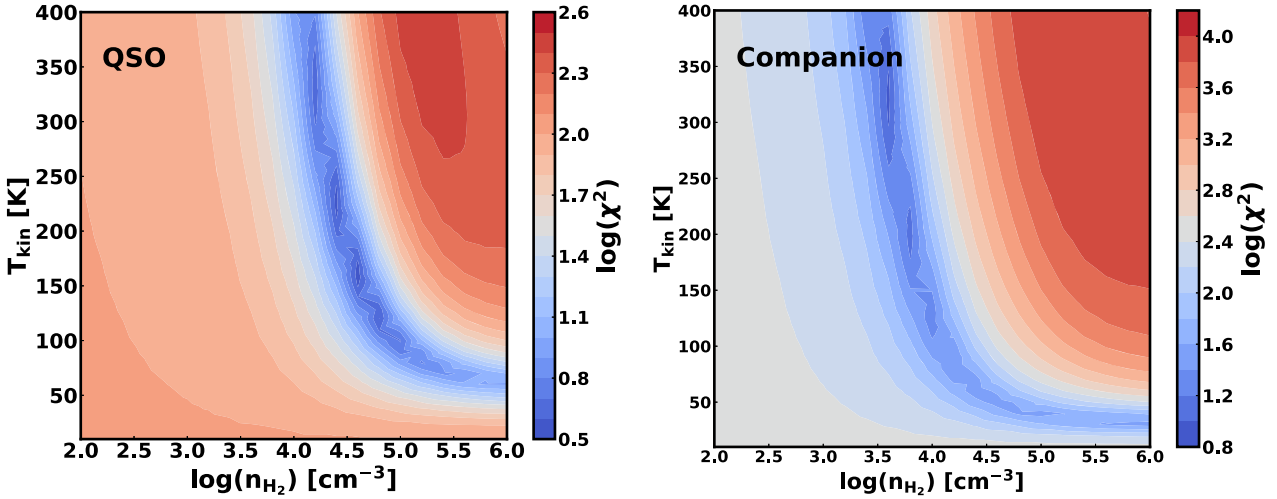

Figure 6. χ^2 contour plots of SMM J04135+10277. The contour plots trace the χ^2 value of the RADEX CO models as a function of molecular hydrogen density and temperature. The left-hand panel shows the fitting results of the quasar and the right-hand panels shows the same for the companion galaxy.

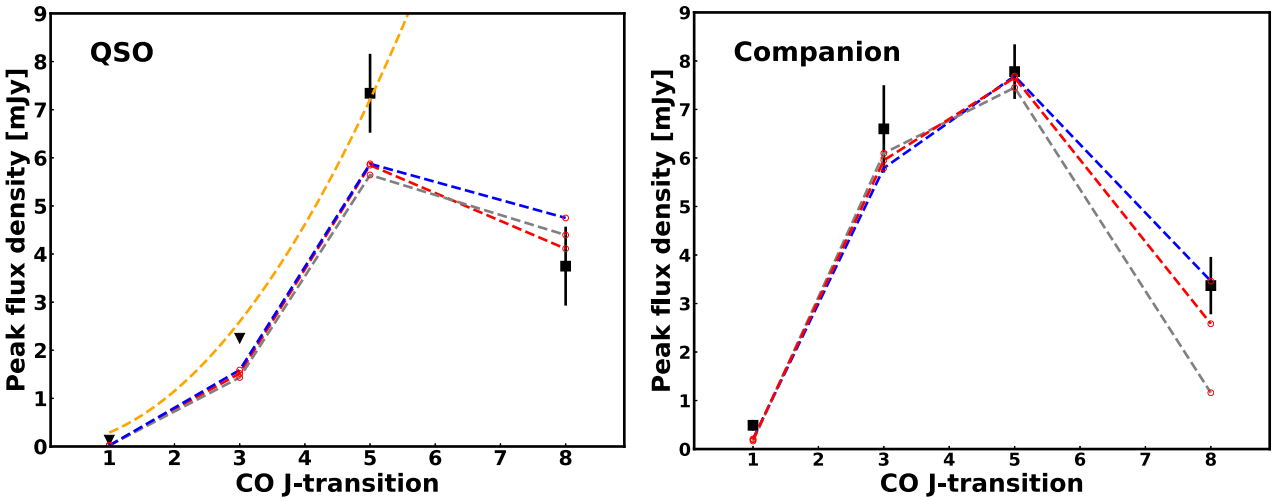

Figure 7. Spectral line energy distribution of SMM J04135+10277. The left-hand panel shows the RADEX SLED fitting of the quasar. We selected three different temperature models with low χ^2 value. The blue, red, and grey curves correspond to models with a $T_{kin} = [360, 160, 100]$ K and $\log(n) = [4.2, 4.6, 5.0]$ cm^{-3}, respectively. The yellow dashed line indicates the J^2 scaling, the expected scaling of the fluxes in the Rayleigh–Jeans limit and in case of thermal excitation. The right-hand panel shows the same for the companion galaxy. The blue, red, and grey curves correspond to models with a $T_{kin} = [530, 300, 110]$ K and $\log(n) = [3.4, 3.6, 4.0]$ cm^{-3}, respectively.

temperature increases with infrared luminosity (Casey et al. 2012). Thus, the infrared luminosities and SFRs of the quasar and the companion estimated from the MR-MOOSE models can be considered as lower limits, and a better sampling around the peak of the SEDs is required to get the whole picture.

Another important note about the FIR SED of the quasar is the possible contribution of the AGN to the total FIR emission. Several studies addressed this question with contradicting results and this topic is still highly debated (e.g. Schweitzer et al. 2006; Leipski et al. 2014; Schneider et al. 2015; Lutz et al. 2016; Symeonidis 2017). What can be assumed based on these studies is that the most luminous AGNs can have a significant contribution to IR emission, mostly at near- and mid-IR wavelength originating from the dusty torus component of AGNs. The main obstacle, which needs to be eliminated is the resolution factor, as many studies use large beam *Herschel* observations, thus potentially detect dust emission from blended sources. Since in our case the dust emission of SMM J04135 is only resolved in the ALMA bands, it is very difficult to estimate the AGN contribution at lower wavelength, in the SCUBA bands in particular.

4.2 Rotation of a massive system

The observed CO(5–4) and CO(8–7) lines of the companion are very broad, with about a 1000 km s^{-1} FWHM in each band. These values are much higher compared to lower J transitions reported in the literature (Riechers 2013; Sharon et al. 2016). Looking at other high-z sources, only a few submm galaxies and quasars have been reported to have such broad CO lines (Genzel et al. 2003; Neri et al. 2003; Greve et al. 2005; Coppin et al. 2008; Polletta et al. 2011; Frayer et al. 2018), making the companion galaxy special.

In order to find the reason of observing such a broad line, we obtained the kinematics of the companion galaxy through velocity maps, velocity dispersion maps and PV diagrams. Based on our

analysis we found no features characteristic to molecular outflows and the velocity map of the companion suggests rotation of a massive and compact galaxy with maximal velocity values of $|V_{\rm max}\ \sin i| \gtrsim 300\,{\rm km\,s^{-1}}$. The velocity dispersion map shows an almost uniform dispersion all over the companion galaxy, which could be an indication of spatially unresolved rotation (Gnerucci et al. 2011).

As we did not find signs of outflows, we consider two possible explanations for the origin of the broad CO lines, which can happen separately or at the same time. The broad line could be the result of not having sufficient resolution to map the companion galaxy and observe the velocity gradients both at large and small scales. Beam smearing has been known as one of the main effects causing broad lines and increasing the observed dispersion of galaxies (e.g. Teuben 2002; Newman et al. 2013; De Breuck et al. 2014; Harborne et al. 2019). At high-z this effect can be even more prominent. As the ALMA beam sizes of our observations are comparable of the CO size of the companion galaxy, this effect is a plausible explanation for observing such broad lines.

Even if the broad line is consistent with rotation, another reason why the observed CO lines are broad could be turbulence, as it has been found in case of recent studies of high-z galaxies (e.g. Gnerucci et al. 2011; Williams et al. 2014). Turbulence could arise from several components, such as having a hidden AGN or from a late stage merger event in the companion galaxy, where the merging galaxies are in coalescence. Given the high SFR of the companion galaxy, the supernova rate might be also high, thus the kinematic energy released by supernovae could also account for part of the turbulence. To investigate these scenarios, higher resolution observation are required, preferably tracing even higher J transitions as well.

4.3 CO excitation properties of SMM J04135+10277

The detection of CO(5–4) and CO(8–7) line emission in both sources complemented with low-J CO observations provides the opportunity to infer the excitation properties of this system. However, there are still some limitations to get the whole picture about the excitation conditions, such as having too few data points to fit the SLED. In case of the quasar, we only have detections in the ALMA bands and upper limits for the CO(1–0) and CO(3–2) emission. This of course affects the χ^2-analysis and thus the RADEX models with low χ^2 value yield very different solutions.

In addition to lacking enough data points, another reason we cannot fit well the observations might be the model itself. By using a model with a more complex radiation field and geometry other than spherical could change the outcome and better fit the data. It has been shown that high-J transitions starting from $J = 7$ are better fitted with models including X-ray dominated regions (XDR; Meijerink, Spaans & Israel 2007). Such models could be especially relevant for the quasar, where the central compact region maybe better modelled by an XDR, while the more diffuse gas associated with star formation is better modelled by a PDR (Meijerink & Spaans 2005). However, models including XDRs have more fitted parameters than the RADEX model used in this paper, and thus could be done provided the SLED was better sampled including more data for $J > 8$ transitions.

The detection of highly excited molecular gas in the host galaxy of the quasar shows that one has to be careful when interpreting non-detections of low-J CO transitions in such sources. For example, Kakkad et al. (2017) presented CO(2–1) observations of $z \sim 1.5$ quasars, with a detection rate of only 30 per cent. Based on our results we note that the low detection rate could be related to the compactness of the CO emitting regions and also because the excitation conditions favour the excitation of high-J transitions, rather than the absence of a massive molecular gas reservoir.

The situation is not less complicated when we look at the SLED of the companion galaxy. While we have four CO detections, it is clear that the companion cannot be fitted with a single-phase component. In the case of SMGs, it has been already demonstrated that their SLED is often best modelled with a combination of an extended, diffuse component and a compact component with higher excitation (Harris et al. 2010; Riechers et al. 2011a; Hodge et al. 2013). However, by fitting two separate components to the low- and high-J CO transitions we encounter the same problem, such as having two observations and two fitted parameters. Therefore, we cannot infer both the temperature and density of the sources.

4.4 Quasar–star-forming companion systems

In recent years, many high-redshift quasars have been observed with ALMA taking advantage of its sensitivity and high resolution. While some of these studies, tracing dust and molecular gas emission, found vigorous star formation and huge gas reservoirs in the host galaxies of the quasars (e.g. Wang et al. 2013; Banerji et al. 2017), the number of detected quasar–star-forming companion galaxy systems has also been growing (e.g. Banerji et al. 2017; Carniani et al. 2017; Decarli et al. 2017; Trakhtenbrot et al. 2017). This is in agreement with our simulation results reported in Fogasy et al. (2017), where we used GALFORM (Gonzalez-Perez et al. 2014; Lagos et al. 2014), a galaxy formation and evolution model to investigate the expected frequency of finding systems similar to SMM J04135+10277. According to the simulations, at a distance of < 350 kpc, 33 per cent of the simulated quasar sample have a companion galaxy ($M_\star > 10^8\,{\rm M_\odot}$) and 2.4 per cent have bright companions with an SFR $> 100\,{\rm M_\odot\,yr^{-1}}$.

However, the system of SMM J04135+10277 seems to differ from the other detected quasar–companion pairs, as the dust emission and the SFR is dominated by the companion.[1] This could be due to the different redshifts of the studied sources, but it might indicate that the companion galaxy of SMM J04135+10277 harbours a hidden AGN, which also has a contribution to the FIR emission. SMGs harbouring hidden AGNs is not a new concept, and in some sources, X-ray observations have already revealed obscured AGNs (e.g. Alexander et al. 2003; Borys et al. 2005). Although both *Chandra* and *XMM–Newton* have observed the field, the observations targeted the foreground X-ray bright galaxy cluster making it difficult to resolve and disentangle emission from the QSO and companion.

Another possible explanation why we do not see many more systems reminiscent of SMM J04135+10277 is the time-scale issue: it could be that we captured the system of SMM J04135+10277 at a special time of its evolution, with the companion galaxy having an intense star-forming phase and the quasar being active. Given the short duration of the starburst phase ($< 10^8$ yr) and quasar lifetime ($< 10^{8.5}$ yr; Di Matteo et al. 2008; Hopkins et al. 2008), it might be

[1]We note that while SFRs of the sources are comparable based on the MR-MOOSE analysis, which makes SMM J04135+10277 more similar to other AGN–companion systems, given the few detections a complete SED fitting is challenging. Thus, we treat the MR-MOOSE values as lower limits to the SFR.

that we simply missed this window of time in case of other known systems and observed them in a later stage of their evolution.

5 CONCLUSIONS

We have presented ALMA observations of the dust continuum, CO(5–4) and CO(8–7) line emission of the quasar–companion galaxy system SMM J04135+10277 ($z = 2.84$). Compared to previous studies of the system using large beam observations, we resolve the continuum emission and detect dust emission associated with both sources. Based on the ALMA continuum data, the dust emission is dominated by the star-forming companion galaxy but the quasar has a non-negligible contribution of 25 per cent to the total emission. We fitted the SED of the sources using the SED fitting code MR-MOOSE, which is designed to treat upper limits and blended sources using a Bayesian approach. Based on the SED fitting the dust temperature of the quasar is higher compared to that of the companion, resulting in similar FIR luminosities for each source.

As the companion galaxy shows a very broad line profile in both CO transitions ($\sim 1000\,\mathrm{km\,s^{-1}}$), we studied the kinematics of the galaxy. The ALMA results show signs of rotation, however, in the absence of high-resolution observations a proper analysis of the kinematics is not possible and the observed line width of the companion is possibly affected by beam smearing.

While previous observations of the CO(1–0) and CO(3–2) transitions only detected molecular line emission associated with the companion galaxy, we detect a significant molecular gas reservoir in each source. The estimated molecular gas mass of the companion galaxy and the quasar host is $\sim 7 \times 10^{10}$ and ~ 0.7–$2.3 \times 10^{10}\,\mathrm{M_\odot}$, assuming a conversion factor of $\alpha_{\mathrm{CO}} = 0.8\,\mathrm{M_\odot}\,(\mathrm{K\,km\,s^{-1}\,pc^2})^{-1}$. In the light of our observations, it is clear that the quasar is not gas-poor as it was suggested by previous studies and has a significant molecular gas mass, only visible at higher frequencies due to excitation.

Using the results of low-J CO transition observations found in the literature and our ALMA CO(5–4) and CO(8–7) detections, we model the SLED of each source using the radiative transfer code RADEX. In the case of the quasar we only have limited amount of detections, thus the model cannot constrain well the excitation properties of the source. However, models with low χ^2 value could narrow down the possible temperature and density range. For the companion the RADEX models cannot put constraints on the temperature but give a consistent estimate for the molecular hydrogen density. The reason of this might be the limited number of observations and the simplicity of the model.

Finally, we compared the case of SMM J04135+10277 to other quasar–companion systems observed by ALMA. In comparison, SMM J04135+10277 stands out from similar systems as the quasar does not dominate the dust emission, while still having a significant amount of molecular gas.

ACKNOWLEDGEMENTS

We thank the anonymous reviewer for the constructive report that helped us to improve the manuscript. JF would like to thank Sabine König for her help and valuable expertise of ALMA data reduction. JF would like to thank Alessandro Romeo, John H. Black, and Susanne Aalto for the useful discussions. JF acknowledges support from the Nordic ALMA Regional Centre (ARC) node based at Onsala Space Observatory. The Nordic ARC node is funded through Swedish Research Council, Grant No. 2017-00648. JF and KK acknowledge support from the Knut and Alice Wallenberg Foundation. KK acknowledges support from the Swedish Research Council. LF acknowledges the support from the National Natural Science Foundation of China (NSFC, Grant Nos. 11822303 and 11773020). This paper makes use of the following ALMA data: ADS/JAO.ALMA#2015.1.00661.S. ALMA is a partnership of ESO (representing its member states), NSF (USA), and NINS (Japan), together with NRC (Canada), NSC and ASIAA (Taiwan), and KASI (Republic of Korea), in cooperation with the Republic of Chile. The Joint ALMA Observatory is operated by ESO, AUI/NRAO, and NAOJ.

REFERENCES

Aird J. et al., 2010, MNRAS, 401, 2531
Aird J., Coil A. L., Georgakakis A., Nandra K., Barro G., Pérez-González P. G., 2015, MNRAS, 451, 1892
Alexander D. M. et al., 2003, AJ, 125, 383
Banerji M., Carilli C. L., Jones G., Wagg J., McMahon R. G., Hewett P. C., Alaghband-Zadeh S., Feruglio C., 2017, MNRAS, 465, 4390
Banerji M., Jones G. C., Wagg J., Carilli C. L., Bisbas T. G., Hewett P. C., 2018, MNRAS, 479, 1154
Bernhard E., Mullaney J. R., Daddi E., Ciesla L., Schreiber C., 2016, MNRAS, 460, 902
Bonfield D. G. et al., 2011, MNRAS, 416, 13
Borys C., Smail I., Chapman S. C., Blain A. W., Alexander D. M., Ivison R. J., 2005, ApJ, 635, 853
Bouché N., Carfantan H., Schroetter I., Michel-Dansac L., Contini T., 2015, AJ, 150, 92
Carilli C. L., Walter F., 2013, ARA&A, 51, 105
Carilli C. L. et al., 2001, ApJ, 555, 625
Carilli C. L., Riechers D., Walter F., Maiolino R., Wagg J., Lentati L., McMahon R., Wolfe A., 2013, ApJ, 763, 120
Carniani S. et al., 2017, A&A, 605, A105
Casey C. M. et al., 2012, ApJ, 761, 140
Chary R., Elbaz D., 2001, ApJ, 556, 562
Coppin K. E. K. et al., 2008, MNRAS, 389, 45
De Breuck C. et al., 2014, A&A, 565, A59
Decarli R. et al., 2017, Nature, 545, 457
Decarli R. et al., 2018, ApJ, 854, 97
Di Matteo T., Springel V., Hernquist L., 2005, Nature, 433, 604
Di Matteo P., Bournaud F., Martig M., Combes F., Melchior A.-L., Semelin B., 2008, A&A, 492, 31
Di Teodoro E. M., Fraternali F., 2015, MNRAS, 451, 3021
Dong X. Y., Wu X.-B., 2016, ApJ, 824, 70
Downes D., Solomon P. M., 1998, ApJ, 507, 615
Drouart G., Falkendal T., 2018, MNRAS, 477, 4981
Duras F. et al., 2017, A&A, 604, A67
Epinat B., Amram P., Balkowski C., Marcelin M., 2010, MNRAS, 401, 2113
Fan L., Knudsen K. K., Fogasy J., Drouart G., 2018, ApJ, 856, L5
Fogasy J., Knudsen K. K., Lagos C. D. P., Drouart G., Gonzalez-Perez V., 2017, A&A, 597, A123
Frayer D. T., Maddalena R. J., Ivison R. J., Smail I., Blain A. W., Vanden Bout P., 2018, ApJ, 860, 87
Gebhardt K. et al., 2000, ApJ, 539, L13
Genzel R., Baker A. J., Tacconi L. J., Lutz D., Cox P., Guilloteau S., Omont A., 2003, ApJ, 584, 633
Gnerucci A. et al., 2011, A&A, 528, A88
Gonzalez-Perez V., Lacey C. G., Baugh C. M., Lagos C. D. P., Helly J., Campbell D. J. R., Mitchell P. D., 2014, MNRAS, 439, 264
Greve T. R. et al., 2005, MNRAS, 359, 1165
Hainline L. J., Scoville N. Z., Yun M. S., Hawkins D. W., Frayer D. T., Isaak K. G., 2004, ApJ, 609, 61
Harborne K. E., Power C., Robotham A. S. G., Cortese L., Taranu D. S., 2019, MNRAS, 483, 249
Häring N., Rix H.-W., 2004, ApJ, 604, L89

Harris A. I., Baker A. J., Zonak S. G., Sharon C. E., Genzel R., Rauch K., Watts G., Creager R., 2010, ApJ, 723, 1139
Hodge J. A. et al., 2013, ApJ, 768, 91
Hopkins P. F., Hernquist L., Cox T. J., Di Matteo T., Robertson B., Springel V., 2006, ApJS, 163, 1
Hopkins P. F., Hernquist L., Cox T. J., Kereš D., 2008, ApJS, 175, 356
Hopkins A. M., 2004, ApJ, 615, 209
Kakkad D. et al., 2017, MNRAS, 468, 4205
Knudsen K. K., van der Werf P. P., Jaffe W., 2003, A&A, 411, 343
Komatsu E. et al., 2011, ApJS, 192, 18
Lagos C. D. P., Baugh C. M., Zwaan M. A., Lacey C. G., Gonzalez-Perez V., Power C., Swinbank A. M., van Kampen E., 2014, MNRAS, 440, 920
Lee N. et al., 2013, ApJ, 778, 131
Leipski C. et al., 2014, ApJ, 785, 154
Lutz D. et al., 2010, ApJ, 712, 1287
Lutz D. et al., 2016, A&A, 591, A136
McConnell N. J., Ma C.-P., 2013, ApJ, 764, 184
McMullin J. P., Waters B., Schiebel D., Young W., Golap K., 2007, in Shaw R. A., Hill F., Bell D. J., eds, ASP Conf. Ser. Vol. 376, Astronomical Data Analysis Software and Systems XVI. Astron. Soc. Pac., San Francisco, p. 127
Madau P., Pozzetti L., Dickinson M., 1998, ApJ, 498, 106
Magorrian J. et al., 1998, AJ, 115, 2285
Maiolino R. et al., 2005, A&A, 440, L51
Marconi A., Hunt L. K., 2003, ApJ, 589, L21
Meijerink R., Spaans M., 2005, A&A, 436, 397
Meijerink R., Spaans M., Israel F. P., 2007, A&A, 461, 793
Merritt D., Ferrarese L., 2001, ApJ, 547, 140
Mullaney J. R. et al., 2012, MNRAS, 419, 95
Narayanan D. et al., 2010, MNRAS, 407, 1701
Neri R. et al., 2003, ApJ, 597, L113
Netzer H., Lani C., Nordon R., Trakhtenbrot B., Lira P., Shemmer O., 2016, ApJ, 819, 123
Newman S. F. et al., 2013, ApJ, 767, 104
Omont A., Cox P., Bertoldi F., McMahon R. G., Carilli C., Isaak K. G., 2001, A&A, 374, 371
Pitchford L. K. et al., 2016, MNRAS, 462, 4067
Polletta M., Nesvadba N. P. H., Neri R., Omont A., Berta S., Bergeron J., 2011, A&A, 533, A20
Ramasawmy J., Stevens J., Martin G., Geach J. E., 2019, MNRAS, 486, 4320
Richards G. T. et al., 2006, AJ, 131, 2766
Riechers D. A., 2011, ApJ, 730, 108
Riechers D. A., 2013, ApJ, 765, L31
Riechers D. A. et al., 2006, ApJ, 650, 604
Riechers D. A. et al., 2009, ApJ, 703, 1338
Riechers D. A., Hodge J., Walter F., Carilli C. L., Bertoldi F., 2011a, ApJ, 739, L31
Riechers D. A. et al., 2011b, ApJ, 739, L32
Sanders D. B., Soifer B. T., Elias J. H., Madore B. F., Matthews K., Neugebauer G., Scoville N. Z., 1988, ApJ, 325, 74
Santini P. et al., 2012, A&A, 540, A109
Schneider R., Bianchi S., Valiante R., Risaliti G., Salvadori S., 2015, A&A, 579, A60
Schulze A. et al., 2019, MNRAS, 488, 1180
Schweitzer M. et al., 2006, ApJ, 649, 79
Sharon C. E., Riechers D. A., Hodge J., Carilli C. L., Walter F., Weiß A., Knudsen K. K., Wagg J., 2016, ApJ, 827, 18
Silva A., Sajina A., Lonsdale C., Lacy M., 2015, ApJ, 806, L25
Solomon P. M., Downes D., Radford S. J. E., Barrett J. W., 1997, ApJ, 478, 144
Stanley F., Harrison C. M., Alexander D. M., Swinbank A. M., Aird J. A., Del Moro A., Hickox R. C., Mullaney J. R., 2015, MNRAS, 453, 591
Symeonidis M., 2017, MNRAS, 465, 1401
Teuben P. J., 2002, in Athanassoula E., Bosma A., Mujica R., eds, ASP Conf. Ser. Vol. 275, Disks of Galaxies: Kinematics, Dynamics and Peturbations. Astron. Soc. Pac., San Francisco, p. 217
Trakhtenbrot B., Lira P., Netzer H., Cicone C., Maiolino R., Shemmer O., 2017, ApJ, 836, 8
Tremaine S. et al., 2002, ApJ, 574, 740
van der Tak F. F. S., Black J. H., Schöier F. L., Jansen D. J., van Dishoeck E. F., 2007, A&A, 468, 627
Venemans B. P., Walter F., Zschaechner L., Decarli R., De Rosa G., Findlay J. R., McMahon R. G., Sutherland W. J., 2016, ApJ, 816, 37
Wagg J. et al., 2012, ApJ, 752, L30
Wang R. et al., 2013, ApJ, 773, 44
Weiß A., Downes D., Neri R., Walter F., Henkel C., Wilner D. J., Wagg J., Wiklind T., 2007, A&A, 467, 955
Williams R. J., Maiolino R., Santini P., Marconi A., Cresci G., Mannucci F., Lutz D., 2014, MNRAS, 443, 3780
Willott C. J., Bergeron J., Omont A., 2015, ApJ, 801, 123
Zheng X. Z. et al., 2009, ApJ, 707, 1566

APPENDIX A: GALPAK^{3D} MODELLING OF THE COMPANION GALAXY

As described in the main text, the angular resolution of the ALMA data does not allow us for a detailed analysis of the kinematics of the companion galaxy. However, given the velocity gradient seen in both the CO(5–4) and CO(8–7) emission, it is possible that at least a fraction of the data could be represented by a rotating disc. Thus, we carry out a simple analysis of the kinematics, assuming a rotating system, using GalPak^{3D} (Bouché et al. 2015). GalPak^{3D} is a Bayesian parametric tool to constrain galaxy parameters directly from three-dimensional data cubes (Bouché et al. 2015). As an input to GalPak^{3D}, we assume a rotating disc with an exponential brightness distribution and with rotational velocity profile described with an arctan profile $v(r) \propto V_{\rm max} \arctan(r/r_{\rm t})$, where $V_{\rm max}$ is a maximum circular velocity and $r_{\rm t}$ is the turnover radius (Bouché et al. 2015). Using the natural weighted cube, we ran the fitting several times with improved starting values for the Bayesian fitting. We note that we use the default settings as the resolution of the data is insufficient to distinguish between different models and the main goal of this simple analysis is to illustrate the possibility of the companion being a rotating system.

GalPak^{3D} models the companion as a compact source with an effective radius of 3.0 ± 0.04 kpc, velocity dispersion of $285 \pm 4\,{\rm km\,s^{-1}}$, maximum velocity of $955 \pm 5\,{\rm km\,s^{-1}}$, and inclination of $28.2 \pm 0.4^{\circ}$, where the uncertainties reflect the 1σ estimates from the Bayesian fitting itself. While we used the natural weighted data, we also repeated the fitting using the data cubes that were imaged using Briggs weighting with a robust parameter of 0.5 and -1.0 (a lower robust parameter means higher angular resolution but worse sensitivity in the data). The results of these runs are consistent with that of the fitting to the natural weighted data, and the effective radius is in the range of 2–3 kpc, the velocity dispersion is in the range of 200–300 km s^{-1}, the maximum velocity is in the range of 900–960 km s^{-1}, and the inclination in the range of $25-29^{\circ}$ (these ranges are based on the highest and lowest 95 per cent confidence intervals of the resulting parameters for fitting to all three resolutions). Most important is to note that without significantly better angular resolution, it is not possible to properly constrain the inclination and make a proper constraint on the maximum velocity. However, while the maximum velocity of $\sim 900\,{\rm km\,s^{-1}}$ most likely reflects the effect of beam smearing, finding a large velocity dispersion and/or large rotational velocity is not surprising given the compactness and large gas mass of the companion galaxy.

In Fig. A1, we show the moment-0, -1, and -2 maps of the data together with that of the model. In the moment-0 and -2 maps, we see that the model is consistent with the data, but the moment-1 map

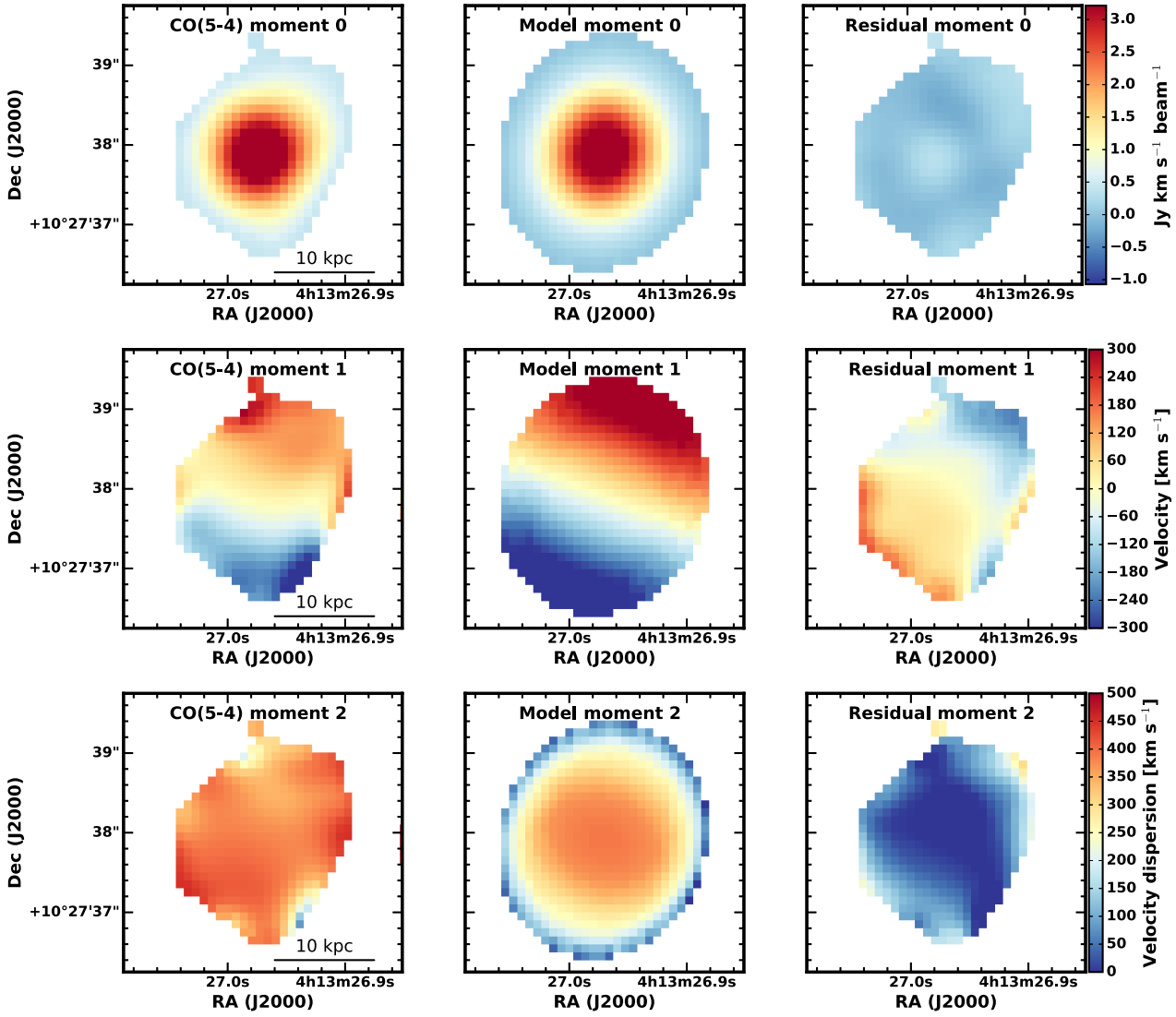

Figure A1. CO(5–4) kinematics of the companion galaxy using the natural weighted data. From left to right, the panels show the derived moment maps of the CO(5–4) data, the GalPak^{3D} model and the residual image. The top panels show the integrated intensity maps, the middle panels show the velocity maps, the bottom panels show the velocity dispersion maps.

shows some velocity residuals. While it is possible to make a model description of a rotating system for the companion galaxy, high angular resolution data are necessary in order to fully characterize the kinematics.

APPENDIX B: KINEMATICS OF THE QUASAR

As the quasar is very compact and unresolved in our observations and there is no signature of a velocity gradient, we do not carry out a GalPak^{3D} analysis, as was done for the companion. In Fig. B1, we show the velocity (moment-1) and velocity dispersion (moment-2) maps of the quasar in the case of both transitions. All maps have been cut to the 3σ level of the moment-0 map.

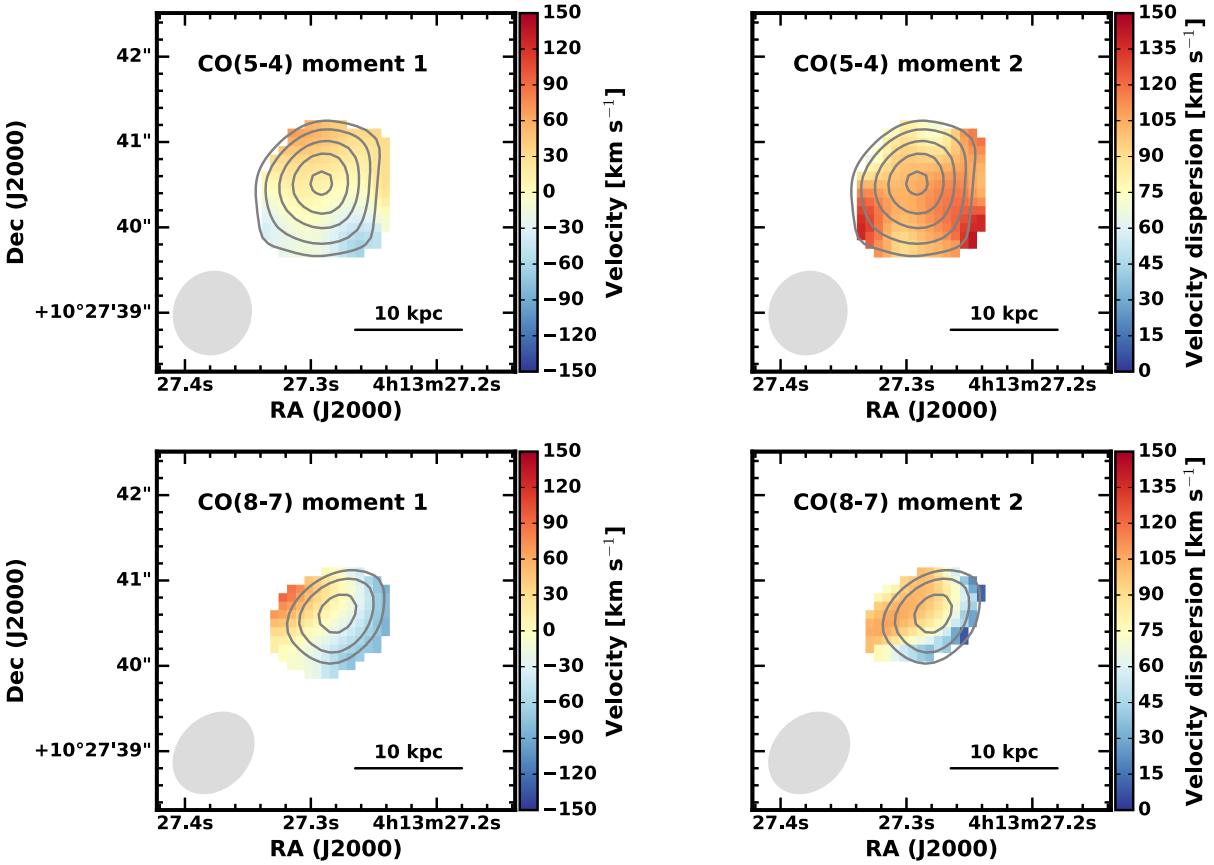

Figure B1. Moment maps of the quasar. *Left:* The velocity map of the quasar. *Right:* The velocity dispersion map of the quasar. Top and bottom rows show the results for the CO(5–4) and the CO(8–7) line, respectively. Contours trace the integrated line intensity with contour levels same as in Fig. 3 for the CO(5–4) emission and Fig. 4. for the CO(8–7) emission. ALMA beams are shown as grey ellipses at the bottom left corner.

This paper has been typeset from a TEX/LATEX file prepared by the author.